Available online at www.sciencedirect.com
ScienceDirect
International Journal of Heat and Fluid Flow 29 (2008) 460–478
International Journal of HEAT AND FLUID FLOW
www.elsevier.com/locate/ijhff

A first assessment of the NEPTUNE_CFD code: Instabilities in a stratified flow comparison between the VOF method and a two-field approach

Yann Bartosiewicz *, Jérôme Laviéville, Jean-Marie Seynhaeve [1]

Université Catholique de Louvain (UCL), Faculty of Applied Sciences, Mechanical Engineering Department, TERM Division, Place du Levant 2, 1348 Louvain-la-Neuve, Belgium

Received 16 January 2007; received in revised form 27 July 2007; accepted 20 September 2007
Available online 5 November 2007

Abstract

This paper presents some results concerning a first benchmark for the new European research code for thermal hydraulics computations: NEPTUNE_CFD. This benchmark relies on the Thorpe experiment to model the occurrence of instabilities in a stratified two-phase flow. The first part of this work is to create a numerical trial case with the VOF approach. The results, in terms of time of onset of the instability, critical wave-number or wave phase speed, are rather good compared to linear inviscid theory and experimental data. Additional numerical tests showed the effect of the surface tension and density ratio on the growing dynamics of the instability and the structure of the waves. In the second part, a code to code (VOF/multi-field) comparison is performed for a case with zero surface tension. The results showed some discrepancies in terms of wave amplitudes, growing rates and a time shifting in the global dynamics. Afterward, two surface tension formulations are proposed in the multi-field approach. Both formulations provided similar results. The time for onset of the instability, the most amplified wave-number and its amplitude were in rather good agreement with the linear analysis and VOF results. However, the time-shifted dynamics was still observed.

Keywords: Two-phase flows; Free surface flows; VOF method; Multi-field method; Surface tension implementation; Code assessment

1. Introduction

The European project Nuclear Reactor SIMulation (NURESIM) aims at developing and validating a numerical platform to model complex multiphase flows, relevant to nuclear reactor thermal hydraulics. In this way, the NEPTUNE_CFD code has been developed within the framework of the EDF-CEA co-development project with the support of AREVA-NP and IRSN. One of the issues of NURESIM project is to set up relevant benchmarks in order to assess the code potentials for a variety of situations encountered in nuclear reactors. Among these situations, safety related flows are those that are more complex and of great interest. One of the possible scenarios (Fig. 1) is cold water emergency core cooling (ECC) into the cold leg during a loss of coolant accident (LOCA). A relevant problem occurring in this situation is the development of wavy stratified flows which may be single-phase or two-phase depending on the leak size, location, and operating conditions. These instabilities may give rise to Kelvin–Helmholtz structures which may induce a slug situation (Wallis and Dobson, 1973; Tailtel and Ducker, 1976). In two-phase flows situation, the Kelvin–Helmholtz roll-up may capture bubbles that may further condense and cause water hammers (Ansari, 1998).

The proposed benchmark aims at tackling this kind of flows but in the case of immiscible fluids. This simplification allows to deal with two-phase related aspects such as

* Corresponding author. Tel.: +3210472206; fax: +3210452692.
E-mail addresses: yann.bartosiewicz@uclouvain.be (Y. Bartosiewicz), jm.seynhaeve@uclouvain.be (J.-M. Seynhaeve).
[1] Tel.: +3210472233; fax: +3210452692.

0142-727X/$ - see front matter © 2007 Elsevier Inc. All rights reserved.
doi:10.1016/j.ijheatfluidflow.2007.09.005

Nomenclature

F_{s_i} (N m^{-3}) volume surface tension force
$F_{k'\to k}$ (N m^{-3}) volume interphase forces
H (m) channel height
L (m) channel length
g (m s^{-2}) gravity acceleration
k (m^{-1}) wave-number
l (m) channel width
n (–) number of phases
N (–) iteration number
R (–) residue
t (s) time
u (m s^{-1}) longitudinal velocity
x (m) longitudinal direction
y (m) transverse direction
α (–) volume fraction
δ (–) density ratio parameter
κ (m^{-1}) interface curvature
λ (m) wavelength
$\|\lambda\|$ (–) FFT amplitude of the wavelength λ
μ (kg m^{-1} s^{-1}) dynamic viscosity
ρ (kg m^{-3}) density
σ (N m^{-1}) surface tension
ΔU (m s^{-1}) axial velocity difference

Subscripts and Superscripts
0 initial time
1 phase 1
2 phase 2
c critical
i, j, q direction indexes
k kth phase

surface tension, density ratio of the fluids, free surface, and to compare both with a simple inviscid analysis (Chandrasekhar, 1961; Drazin and Reid, 1982) and experimental results. However, the linear inviscid theory is valid for the case of two fluids of similar density (Thorpe, 1969). This problem has been tackled by Meignin et al. (2003) with the nonlinear analysis or by Staquet (1995, 2000) with numerical simulations of a single-phase flow. A review of experiments of Kelvin–Helmholtz instability with large density differences can be found in Funada and Joseph (2001). Concerning the case of two-phase flows with heat and mass transfers, many studies can be found in the literature and they are mostly devoted to the modeling or measurement of interfacial transfers (Lioumbas et al., 2005; Kim et al., 1985; Biberg and Halvorsen, 2000). Moreover, due to the additional difficulty related to the nature of the flow (liquid water–water steam) and the associated modeling issues, this kind of study cannot be used as an objective benchmark to assess the code potential. A possible benchmark could be that of Hou et al. (2001) who analyzed two inviscid fluids of equal density in zero gravity conditions. However, this case is not realistic, and an experimental background is missing. Therefore, the proposed benchmark is the same as that planned in Tiselj et al. (2004) and relies on the work of Thorpe (1969). Indeed, this work is very convenient for the targeted benchmark, because experimental data and matching theoretical results are available for comparison to computational fluid dynamics (CFD) simulations. Recently, Bartosiewicz and Seynhaeve (2006) set up the test case by conducting a first comparison between experimental data, theoretical analysis and a commercial CFD package.

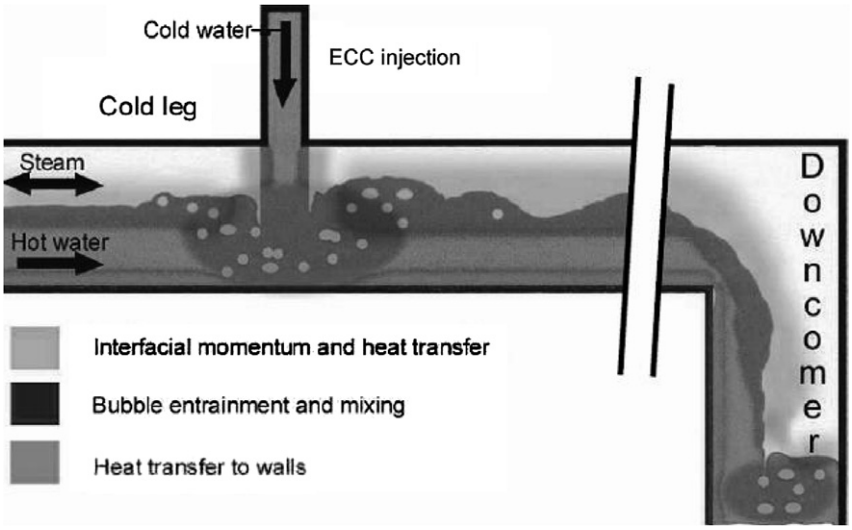

Fig. 1. Cold water emergency core cooling (ECC) into the cold leg during a loss of coolant accident (LOCA).

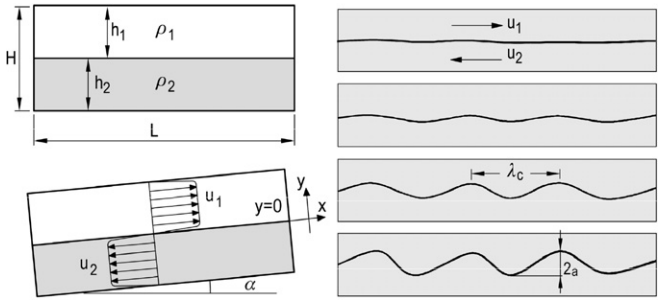

Fig. 2. Description of the Thorpe experiment.

2. Description of the Thorpe experiment and results

2.1. Description of the experiment

The Thorpe experiment (Thorpe, 1969) consists in a glass channel containing two immiscible fluids of different but similar densities (Fig. 2). The fluids were water (fluid 2 at the bottom) and a mixture of tetrachloride and commercial paraffin (fluid 1 at the top) with the following properties:

$$\begin{aligned} &\rho_1 = 780\ \text{kg/m}^3, \quad \mu_1 = 0.0015\ \text{Pa s} \\ &\rho_2 = 1000\ \text{kg/m}^3, \quad \mu_2 = 0.001\ \text{Pa s} \end{aligned} \tag{1}$$

Concerning the geometry parameters, the following dimensions have been used in the experiment:

$$L = 1.8\ \text{m}, \quad H = 0.03\ \text{m}, \quad l = 0.1\ \text{m} \tag{2}$$

Initially, the tube was completely filled with the fluids. Both fluid layers have the same initial height $h_1 = h_2 = 1.5$ cm. The surface tension was estimated to be $\sigma = 0.04$ N/m by measurements with 10% accuracy; however, Thorpe (1969) claimed that errors due to this uncertainty are small in calculations. After allowing the fluids to settle, the channel was sharply tilted such that $\sin\alpha = 0.072$. The resulting motion is a wavy flow giving rise to Kelvin–Helmholtz instabilities. The motion of the interface is recorded from the side and the flow is also filmed from above by means of a mirror. From the theoretical and computational point of view, the tube width is large compared to the thickness of the shear layer, justifying a two-dimensional approach.

2.2. Main experimental results

For the operating conditions mentioned above, Thorpe (1969) took 10 pictures of the interface, separated by 0.059 s (examples in Fig. 3). The first picture is taken at a time when onset of the instability has been observed. This time is 1.88 ± 0.07 s and includes half the time taken to tilt the channel (about 0.25 s). In his paper, Thorpe claims that this uncertainty might be even larger. The most unstable wave number is estimated with the distance between two wave crests (Fig. 2). The measured value is $\lambda_c = 2.5$–4.5 cm, the uncertainty comes from the different critical wavelengths observed under the same operating conditions. After the onset on the instability Thorpe observed the growth of the waves for approximately 0.52 s. Beyond this time, this growth was almost stopped and the roll-up of these waves started. At this time the estimated amplitude of the waves was about $2a = 6$–8 mm (Fig. 2). The downward wave speed was also measured to be 2.6 cm s^{-1}. As far as possible, all these experimental data will be compared to the numerical simulations.

3. Linear inviscid analysis

In this section, we recall some important results of linear-hydrodynamics instability theory, which are of interest to determine criteria for the occurrence of instabilities, and the associated parameters. For a more complete presentation, the reader is referred to Drazin and Reid (1982).

Let us consider an inviscid fluid flow such as

$$\begin{aligned} -h_2 < y < 0 &\begin{cases} \rho = \rho_2 \\ u_2 = -\Delta U/2 \end{cases} \\ 0 < y < h_1 &\begin{cases} \rho = \rho_1 \\ u_1 = \Delta U/2 \end{cases} \end{aligned} \tag{3}$$

with $h_1 = h_2$. This parallel flow is assumed to be a solution of Euler equations upon which is superposed a small perturbation proportional to $\exp i(kx + \omega t)$. In this latter equation, k is real, and it is the longitudinal wave-number of the perturbation; ω is complex where the real part ω_r is the phase speed and the complex part ω_c is the temporal growth rate of the perturbation. Once the two-dimensional

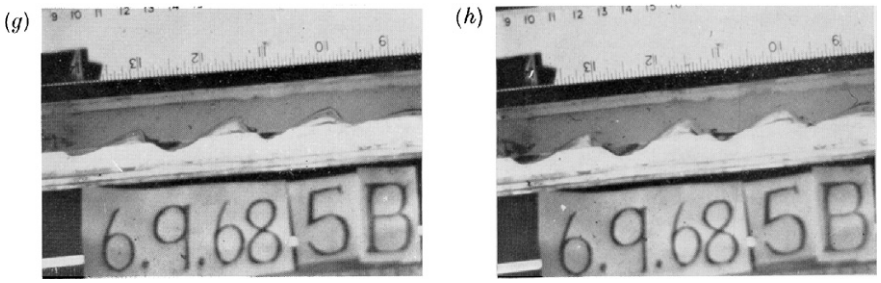

Fig. 3. The Thorpe experiment – Examples of pictures of the interface.

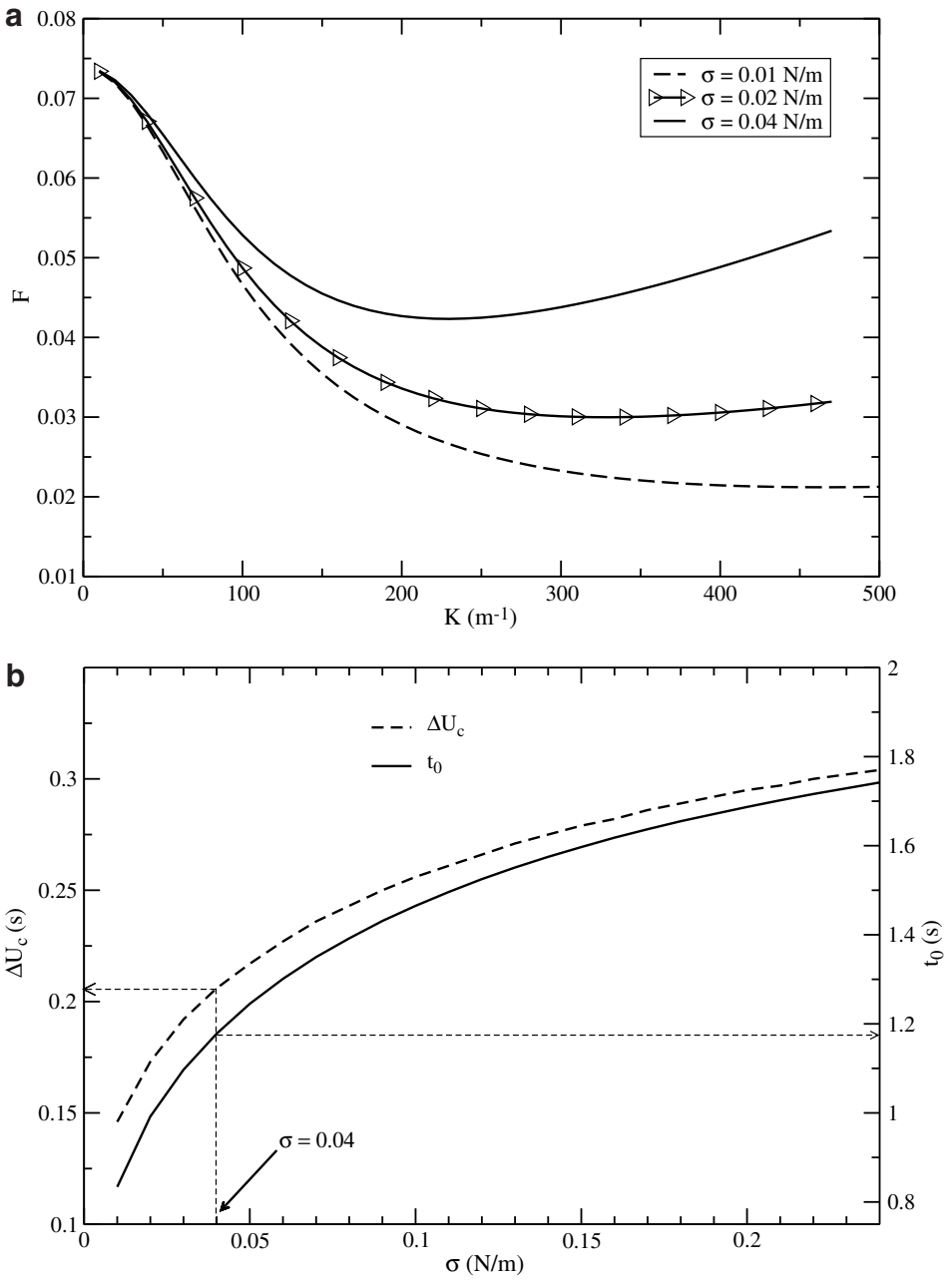

Fig. 4. F as a function of k (a) and critical velocity and time of onset of instability (b).

Euler equations are linearized, the following dispersion relation can be obtained for ω (Chandrasekhar, 1961):

$$\omega = k\frac{\Delta U(\rho_2-\rho_1)}{2(\rho_2+\rho_1)} \pm \sqrt{\frac{\sigma k^3 + gk(\rho_2-\rho_1)}{\rho_2+\rho_1}\tanh(kh) - \frac{k^2(\Delta U)^2\rho_1\rho_2}{(\rho_2+\rho_1)^2}} \quad (4)$$

The system is unstable when $\omega_c \neq 0$, providing a condition for the minimum (critical) velocity difference:

$$(\Delta U)^2 > \frac{\rho_1+\rho_2}{\rho_1\rho_2}\left(\sigma k + \frac{g}{k}(\rho_2-\rho_1)\right)\tanh(kh) \triangleq F \quad (5)$$

Therefore, the minimum of the function F gives the most unstable wave number k_c. This is shown in Fig. 4a for different values of surface tension.

A limiting case of Eq. (5) can be examined corresponding to an infinite height of the channel. In that case, the function F vanishes for the following critical wave-number:

$$k_c \sim \sqrt{\frac{g(\rho_2-\rho_1)}{\sigma}} \quad (6)$$

Moreover, the time-dependent solution of the problem may be easily derived if closed-end and viscosity effects are ne-

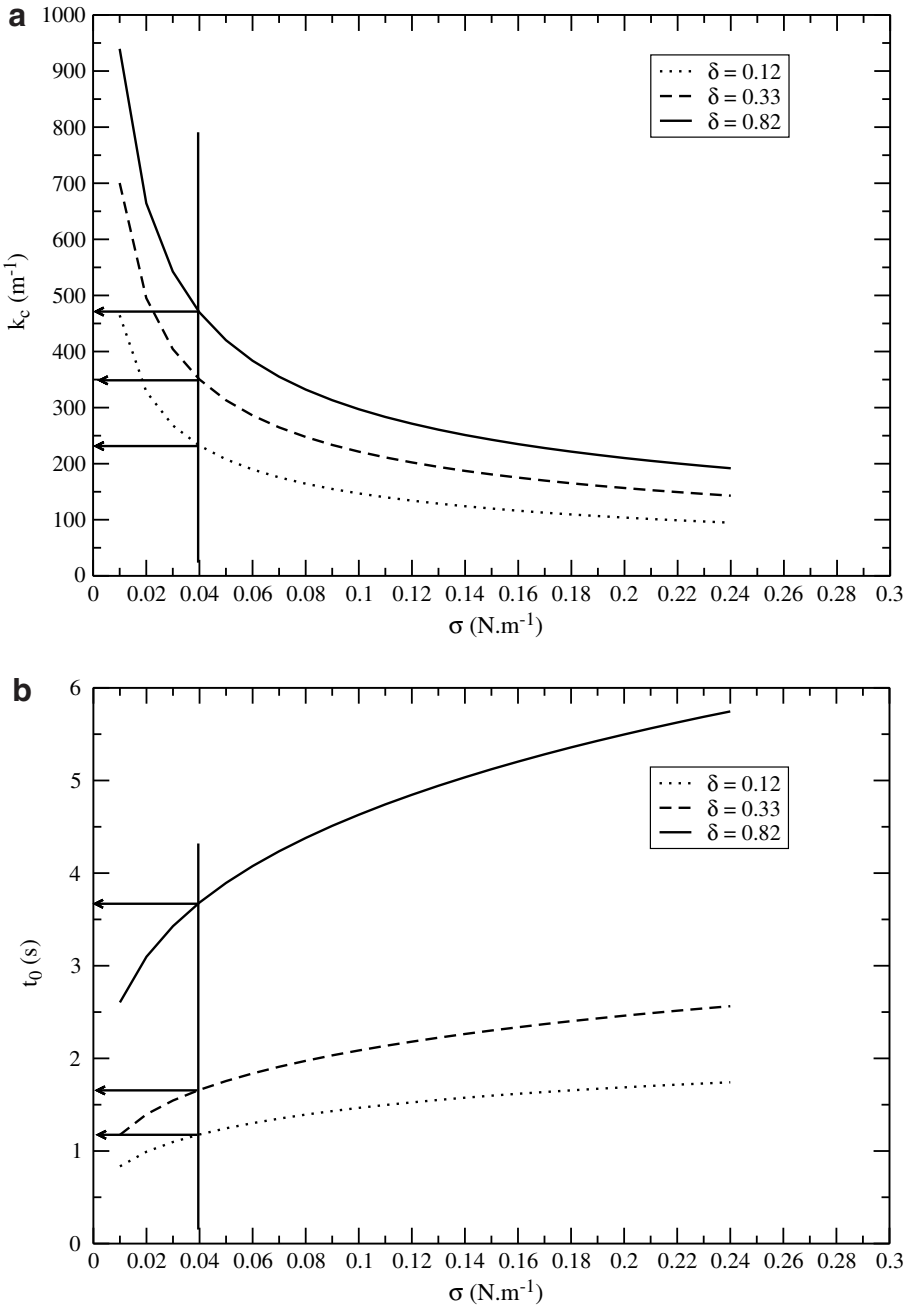

Fig. 5. Wave number (a) and time of onset of instability (b) as a function of the surface tension for different δ.

glected (Thorpe, 1969), and it gives the following velocity field:

$$U = \begin{cases} u_1 = \frac{(\rho_2-\rho_1)h_2 g \sin\alpha}{\rho_1 h_2+\rho_2 h_1} t, & 0 < y < h_1 \\ u_2 = -\frac{(\rho_2-\rho_1)h_1 g \sin\alpha}{\rho_1 h_2+\rho_2 h_1} t, & -h_2 < y < 0 \end{cases} \quad (7)$$

From this equation, it possible to estimate for a given $U = \Delta U_c/2$ corresponding to the minimum of the function F, the time of onset of the instability t_0. In Fig. 4b, the critical velocity difference ΔU_c and the corresponding time t_0 are shown as a function of surface tension.

3.1. Application to the trial case: The Thorpe experiment

In the case of matching geometrical and operating boundary conditions realized in Thorpe's experiment (Thorpe, 1969), this critical wave number is $k_c = 229\ \mathrm{m}^{-1}$ (Fig. 3): this gives a critical wavelength $\lambda_c = 2.7$ cm and a critical velocity difference $\Delta U_c \approx 0.2$ m/s. In his paper, Thorpe claims that the critical velocity and therefore the time of onset of instability predicted by the theory may be underestimated by as much as 10%, because an abrupt transition in velocity is assumed at the interface. However, the minimum of the function F is relatively flat (Fig. 4a),

explaining the reason for several possible critical wave numbers. Moreover, the critical wave number determined by Eq. (6) for the Thorpe experiment is equal to 232.3 m^{-1} which is very close to 229 m^{-1}. This means that the height of the channel used in the Thorpe's experiment is large enough for considering that the height has no influence on the instability.

The benchmark conditions of the trial case are also stressed on the graph of Fig. 4b: for these conditions, the time of onset of the instability is about $t_0 = 1.2$ s for a critical velocity slightly higher than 0.2 m/s. Thorpe found that these results have to be corrected by 10% to take into account the corrections due to viscosity and accelerated flow. For instance, Thorpe evaluated the theoretical time $t_0 = 1.5$–1.7 s including half the time to tilt the channel.

3.2. Effect of surface tension and density ratio

Furthermore, Fig. 4a and b also depicts the influence of the surface tension on the critical velocity difference, the wave number and the time of onset of instability. As surface tension is decreased, the minimum velocity required to get instability is also decreased which means that the time for the onset of these instabilities should be shorter as well. In addition, the minimum of F becomes less sharper as σ is decreased, giving more possibilities of critical wave numbers, and these critical wave numbers increase: this means that the wavelength decreases when the surface tension at the interface decreases. However, according to the linear inviscid theory, in the case of $\sigma = 0$ N m^{-1}, the wave instabilities should appear at the beginning of the transient ($t_0 = 0$ s) as shown in Fig. 4b, but this theory fails when the surface tension tends to zero.

The effect of the density ratio of the fluids can also be investigated from Eqs. (5) and (7). This has been done for different density ratios defined by the parameter δ:

$$\delta = \frac{\rho_2 - \rho_1}{\rho_2 + \rho_1} \tag{8}$$

The results are summarized in Fig. 5a and b for the three values $\delta = 0.12$, 0.33 and 0.82. These values correspond, respectively, to three different densities of the upper fluid, i.e., 780, 500 and 100 kg/m^3, for the same density of the fluid at the bottom (1000 kg/m^3).

According to the linear inviscid theory, Fig. 5a and b shows that the critical wave number as well as the time of onset of the instability increase when the parameter δ decreases. But it must be underlined that this theory is only valid for $\delta \ll 1$ (Thorpe, 1969). Thus, the results shown in Fig. 5a and b must be taken very carefully.

4. Modeling approach

4.1. The VOF approach

The conservation equations governing the fluid flow in the channel are of the incompressible, unsteady, and two-dimensional form. Furthermore, as the point of interest is the formation of Kelvin–Helmholtz instabilities up to their roll-up, and the maximum matching Reynolds Number is about 183 (Thorpe, 1969), only the laminar form of these equations is solved in the present work. The channel is assumed adiabatic and no thermal energy is exchanged between flows, so the energy equation is not solved. As far as two immiscible fluids are concerned, the Euler–Euler VOF technique is suited to track the interface. The governing equations can therefore be written (for $n = 2$):

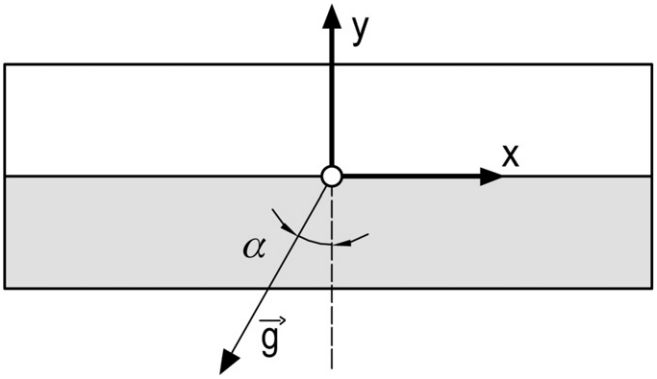

Fig. 6. Computational domain.

$$\frac{\partial \alpha_k \rho_k}{\partial t} + \frac{\partial}{\partial x_i}(\alpha_k \rho_k u_i) = 0 \quad \text{for } k \in [1, n-1] \tag{9}$$

$$\sum_{k=1}^{n} \alpha_k = 1 \tag{10}$$

$$\frac{\partial(\rho u_i)}{\partial t} + \frac{\partial}{\partial x_j}(\rho u_i u_j) = -\frac{\partial P}{\partial x_i} + \frac{\partial \tau_{ij}}{\partial x_j} + \rho g_i + F_{S_i} \tag{11}$$

$$\tau_{ij} = \mu\left(\frac{\partial u_i}{\partial x_j} + \frac{\partial u_j}{\partial x_i}\right) \tag{12}$$

where F_s accounts for the surface tension effect (Brackbill et al., 1992) and its formulation is detailed in Section 5.2.2; the mixture properties are evaluated as $\rho = \sum \alpha_k \rho_k$ and $\mu = \sum \alpha_k \mu_k$. This set of equations is solved with the commercial code FLUENT.

The interface treatment is accomplished via a geometric reconstruction scheme. If a given cell is completely filled with one or the other phase, no special treatment is performed. However, if the interface is included within a cell, it is represented by a linear slope by using piecewise-linear interpolation. The first step in this reconstruction is computing the position of the linear interface in the cell, based on the volume fractions and their derivatives. The second step is calculating convective fluxes through each face of the cell using the computed interface and velocities (normal and tangential) on the face. The final step is to update volume fractions based on the balance of fluxes calculated during the previous step.

The pressure–velocity coupling is realized by using the pressure-implicit with splitting of operators (PISO) algorithm (Issa, 1986) which ensures that the corrected velocities satisfy both the continuity and the momentum

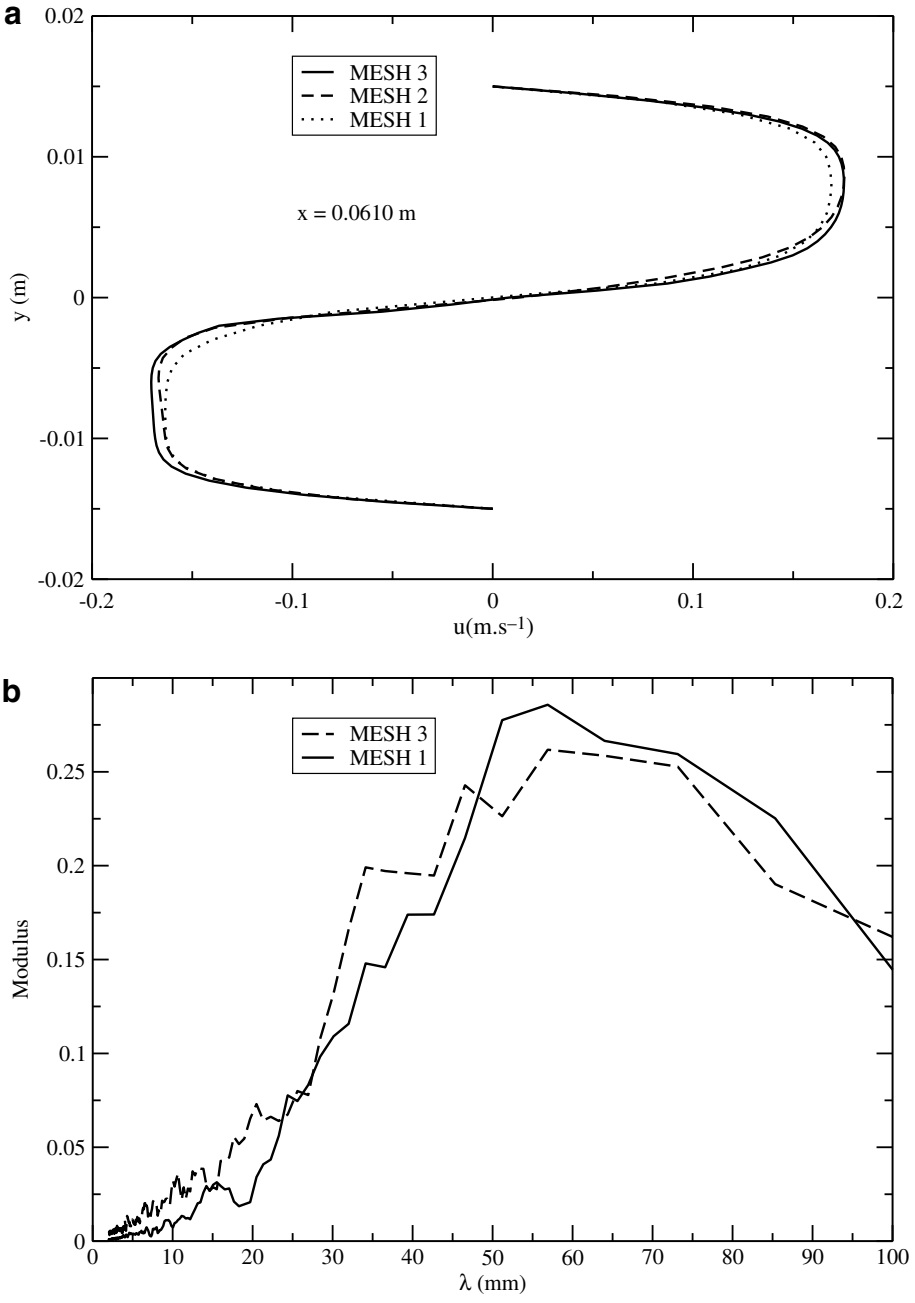

Fig. 7. Grid convergence study.

equations after one or more additional loops. This algorithm takes more CPU time per solver iteration than SIMPLER or SIMPLEC, but it can dramatically decrease the number of iterations required for convergence in transient problems. Spatial discretization is achieved by a QUICK scheme with a staggering technique for the pressure term in the momentum equation. The time discretization uses a first order implicit scheme for flow equations, while an explicit time marching technique is used for the volume fraction equation (Eq. (9)). For the validation calculations (the Thorpe experiment), the global time step is time-adapted in order to ensure a maximum CFL = 1. However, for comparison with NEPTUNE_CFD a constant time step was used in order to obtain results at same times, and ensuring for a maximum CFL = 1 during the computation.

The resulting system is then solved using a point implicit Gauss–Seidel solver in conjunction with an algebraic multigrid method.

4.2. The multi-field approach: NEPTUNE_CFD

In the NEPTUNE_CFD code, the general compressible Eulerian multi-field balance equations are solved. In the case of two components, this two-field/one pressure formu-

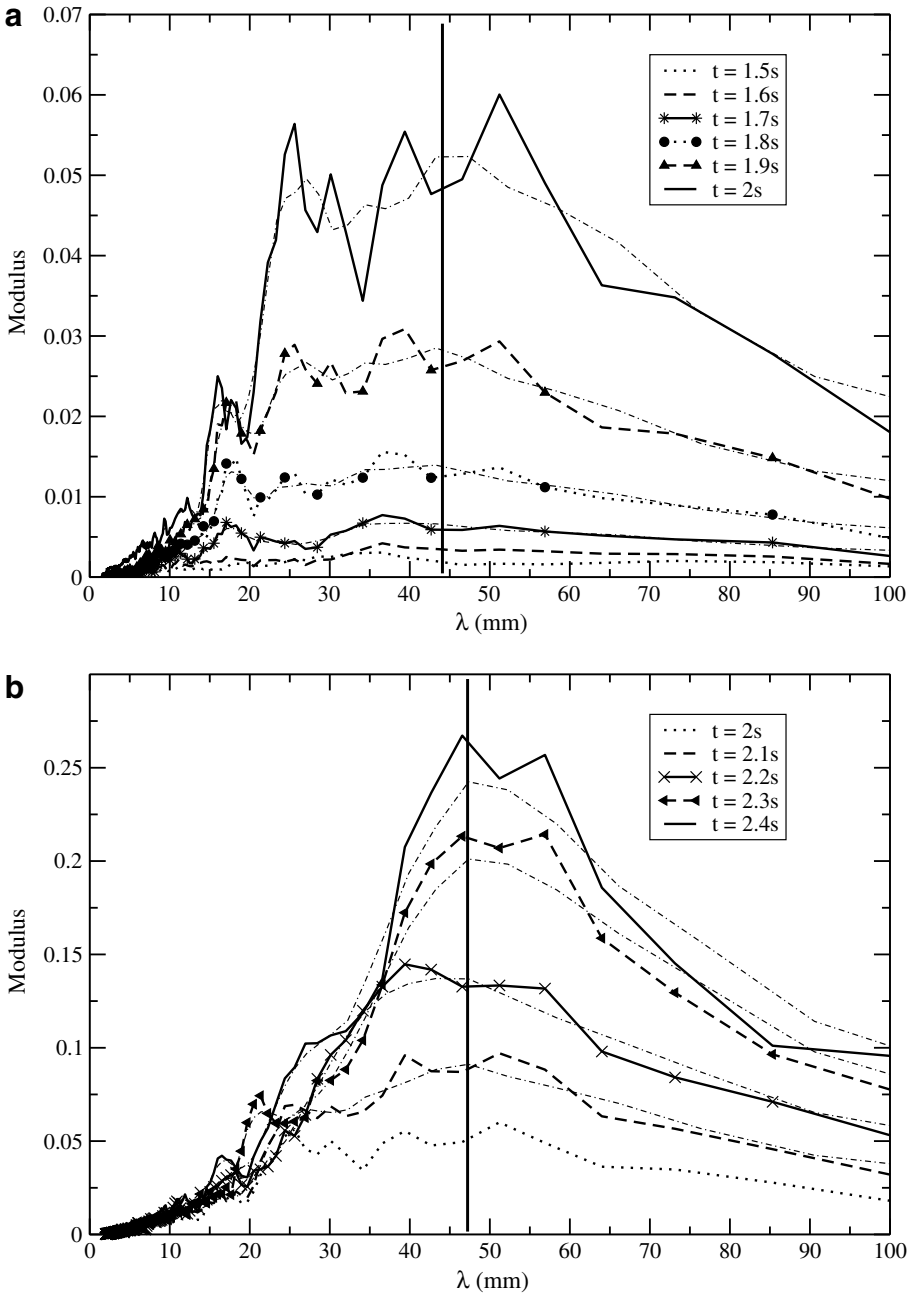

Fig. 8. Fourier analysis of the interface.

lation is actually the classical two-fluid model and can be written for the kth field:

$$\frac{\partial \alpha_k \rho_k}{\partial t} + \frac{\partial}{\partial x_i}(\alpha_k \rho_k u_{k,i}) = 0 \quad \text{for } k \in [1, n-1] \tag{13}$$

$$\sum_k \alpha_k = 1 \tag{14}$$

$$\frac{\partial(\alpha_k \rho_k u_{k,i})}{\partial t} + \frac{\partial}{\partial x_j}(\alpha_k \rho_k u_{k,i} u_{k,j}) = -\alpha_k \frac{\partial P}{\partial x_i} + \frac{\partial \alpha_k \tau_{ij}}{\partial x_j} + \alpha_k \rho_k g_i + F_{k\prime \to k} \tag{15}$$

$$\tau_{ij} = \mu\left(\frac{\partial u_i}{\partial x_j} + \frac{\partial u_j}{\partial x_i}\right) - \frac{2}{3}\frac{\partial u_q}{\partial x_q}\delta_{ij} \tag{16}$$

Consequently, NEPTUNE_CFD solves a complete set of equations for each phase ($k-1$ for the continuity) while one momentum equation is solved for the mixture in the VOF method. The term $F_{k' \to k}$ may include drag models to couple momentum equations. In this work, no specific friction model is included but rather the implicit continuity condition. However, the term $F_{k' \to k}$ will include a specific surface tension formulation for each phase as a coupling term. Indeed, NEPTUNE_CFD, as many multi-field codes, does not usually include surface tension effect since fully separated flows calculations are not in the spirit of such an approach. The detail of the surface tension formulation may be found in Section 5.2.2.

The time integration uses a splitting approach. In a first step, an implicit velocity prediction is made neglecting the volume fractions and pressure variations. However, this prediction is realized from a first sub-step where the momentum equation containing only explicit components (pressure and volume fraction variations) is solved. Using this predicted velocity, several cycles are achieved by solving sequentially the coupled system of energy–volume fraction–pressure equations. This system is solved using sub-cycles until convergence. Velocities are updated at each sub cycle. The second step is the final velocity correction in a similar way in comparison to the SIMPLER algorithm by using the implicit part of the momentum equation. The energy–volume fraction–pressure sub-cycles are stopped when mass and energy conservations are ensured. The use of an elliptic form for the pressure correction equation provides the elliptic feature of the algorithm.

Spatial discretization is achieved by a central difference scheme. All variables are co-located, a gradient reconstruction method providing consistency and precision for diffusive and convective fluxes.

4.3. Domain, boundary and initial conditions

The computational domain is two-dimensional and the dimensions match with those of Thorpe's experiment (Thorpe, 1969). The channel is taken horizontal, but the gravity vector is inclined to model real experimental conditions (Fig. 6). For this geometry, three different orthogonal meshes have been tested in order to check grid convergence:

- MESH 1: 1830×30;
- MESH 2: 2588×42;
- MESH 3: 3660×60.

In the next section, it is shown that MESH 1 was taken for all the simulations.

All boundary conditions are walls with no-slip condition. At $t = 0$, each fluid fills half the height of the channel, so that the interface is initially located along the middle line of the domain. Initially, all velocities equal zero and the pressure field is uniform and equal to the reference pressure (atmospheric pressure): this pressure field does not match with operating conditions since the channel is already tilted in simulations. To ensure a good initial pressure field, a small time ($t = 1 \times 10^{-5}$ s) step is performed in order to make the pressure converge toward its hydrodynamics distribution. At this time, the computation can be started with the required time step.

4.4. Numerical accuracy and convergence

The criterion for assessing convergence was primarily based on the mass residues. In FLUENT, this criterion is the rate of mass creation at iteration N and can be defined as

$$R^N(\alpha) = \sum_{i=1}^{\mathrm{NCEL}} |\dot{m}^i_{\mathrm{in}} - \dot{m}^i_{\mathrm{out}}|_N \tag{17}$$

where $\dot{m}^i_{\mathrm{in}}$ and $\dot{m}^i_{\mathrm{out}}$ are the total inlet mass flow rate penetrating and escaping a cell i, respectively.

In addition, the convergence is monitored and assessed following a scaled residual criterion:

$$\frac{R^N(\alpha)}{R^5(\alpha)} < 1 \times 10^{-4} \tag{18}$$

In NEPTUNE_CFD, the volume fraction–pressure–energy cycles stop once the volume conservation holds in a sub-step:

$$\max_{I \in \mathrm{NCEL}} \left(|1 - \sum_k \alpha_k(I)| \right) < 10^{-5} \tag{19}$$

This criterion is very severe as it applies to a maximum value over the whole domain. In order to assess grid convergence, the three different meshes have been tried out with FLUENT. This independency was then checked in NEPTUNE_CFD by comparing the selected mesh with the next finer mesh, but for conciseness reasons only the results comparing the three meshes are shown. Finally, the chosen mesh was further used both with FLUENT and NEPTUNE_CFD. Fig. 7a illustrates the results in terms of radial profiles of longitudinal velocity component at $t = 2$ s for the three tested meshes. At this time, the instability is well established; the velocity difference $\Delta U \approx 0.35$ m/s is largely higher than the theoretical velocity $\Delta U_c \approx 0.21$ m/s. The three tested meshes do not exhibit significant differences, while the CPU time is multiplied by 4 between MESH 1 and MESH 3. For the finer grid, the capture of the velocity gradient through the shear layer is slightly improved (Fig. 7a). Fig. 7b depicts the Fourier analysis of the interface ($\alpha = 0.5$) for MESH 1 and MESH 3: overall results show that MESH 1 contains the essential spectral information and can be sufficient for this study. Therefore, the coarser mesh MESH 1 was used for all the simulations presented in this paper.

5. Results and discussion

5.1. The Thorpe experiment: the VOF approach

5.1.1. The trial case

Since Thorpe's experiment accounts for the surface tension effect, we decided to create a first trial case in order to check the ability of the VOF model incorporated in FLUENT to model this challenging experiment. Furthermore, this validation provides more rigorous basis for the further comparisons between FLUENT and NEPTUNE_CFD. Fig. 8a and b shows the Fourier analysis of the interface between $t = 1.5$ s and $t = 2.4$ s. Fourier transforms have been obtained with a FFT algorithm and a running average upon five values has been performed. The dash–dot curve represents an additional running average for each FFT.

Fig. 8a illustrates that the time of onset of the instability is $1.6\ \text{s} < t_0 < 1.9\ \text{s}$ because the growing rate seems to become significant between these values. A more exact value of t_0 is evaluated to be $t_0 = 1.86$ s from Fig. 12. This is in accordance with the Thorpe observation $t = 1.88$ s including half the time to tilt the channel ($t_0 = 1.63 \pm 0.07$ s). Moreover, the critical wavelength matching the most unstable wavenumber can be evaluated at $\lambda_c \approx 44$ mm ($k_c = 142.8\ \text{m}^{-1}$) compared to the Thorpe value $\lambda_c = 25$–45 mm ($k_c = 197 \pm 58\ \text{m}^{-1}$). The computed values agree well with the Thorpe observations, because the range of possible critical waves is quite wide (Fig. 8) ($\lambda_c = 25$–55 mm) in accordance with results found in Fig. 4. In addition, it is also observed that this critical wavelength does not much change significantly with time as observed by Thorpe and remains at $\lambda_c \approx 45$ mm. However, Thorpe observed the growing of the wave was almost stopped at $t \approx 2.4$ s. Fig. 8b shows that the growing is slows down between $t \approx 2.3$ s and $t \approx 2.4$ s. Fig. 9 exhibits the location of the physical interface between $t = 1.7$ s and $t = 1.9$ s. The crest-to-crest distance allows to determine the velocity of the wave moving downward. The computed distance for this 0.2 s time period is evaluated to be 0.5 cm, which gives a velocity of $u \approx 2.5\ \text{cm s}^{-1}$: Thorpe evaluated this velocity at $u \approx 2.6\ \text{cm s}^{-1}$.

For summarizing Table 1 presents the different results obtained from CFD in comparison to the linear inviscid theory, corrections of the theory proposed by Thorpe, and the experimental results obtained by Thorpe. It is clear that the time of onset of instabilities, the wave speed, and also the critical velocity difference (obtained at t_0) are in rather good agreement with both theory and Thorpe data. Nevertheless, the critical wavelength is overestimated in comparison with the linear theory for both CFD results and the Thorpe data. In addition, corrections should lower the theoretical value. This discrepancy may be attributed to the finite amplitude effect that could be important at the early stage of wave development and not taken into account in the current theory. Moreover, Thorpe suggests that Kelvin–Helmholtz instability is probably dominant but the occurrence of Tollmien–Schlichting instability could be envisaged at the interface.

Table 1
Comparison between theory, the Thorpe data and CFD (FLUENT) results

Parameter	Theory	Theory (corrected) (Thorpe)	Thorpe	FLUENT
k_c	$229\ \text{m}^{-1}$	$320\ \text{m}^{-1}$	$140\ \text{m}^{-1}$–$251\ \text{m}^{-1}$	$142\ \text{m}^{-1}$
λ_c	2.7 cm	1.96 cm	2.5–4.5 cm	4.4 cm
t_0	1.2 s	1.5–1.7 s	$1.88\ \text{s} \pm 0.07$ s	1.86 s
ΔU_c	$0.21\ \text{m s}^{-1}$	$0.22\ \text{m s}^{-1}$	–	$0.28\ \text{m s}^{-1}$
v_{waves}	$2.38\ \text{m s}^{-1}$	–	$2.6\ \text{m s}^{-1}$	$2.5\ \text{m s}^{-1}$

5.1.2. Effect of surface tension

In order to assess the effect of surface tension on the development of waves, a case with zero surface tension has been performed. From the linear inviscid theory, the most unstable wavelength should decrease as surface tension is decreased (Fig. 4a). In addition, the minimum of function F (Fig. 4a) becomes more and more flat, which means that the number of critical wavelengths increases; for zero surface tension infinity wave-numbers are predicted. However, the theory becomes inaccurate as the surface tension decreases (Thorpe, 1969) and should be taken with care, especially at zero surface tension. Fig. 10 shows

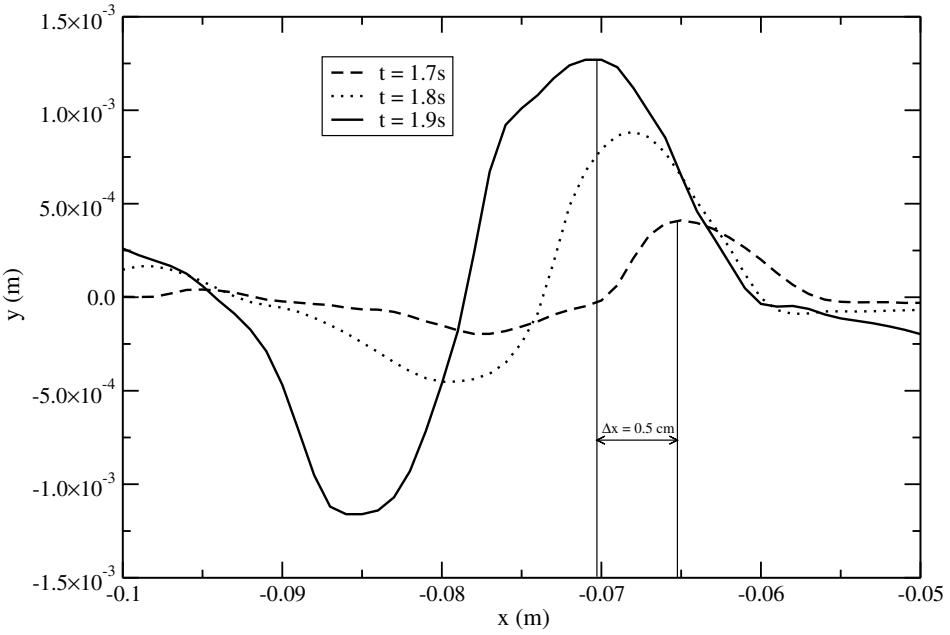

Fig. 9. Physical location of the interface.

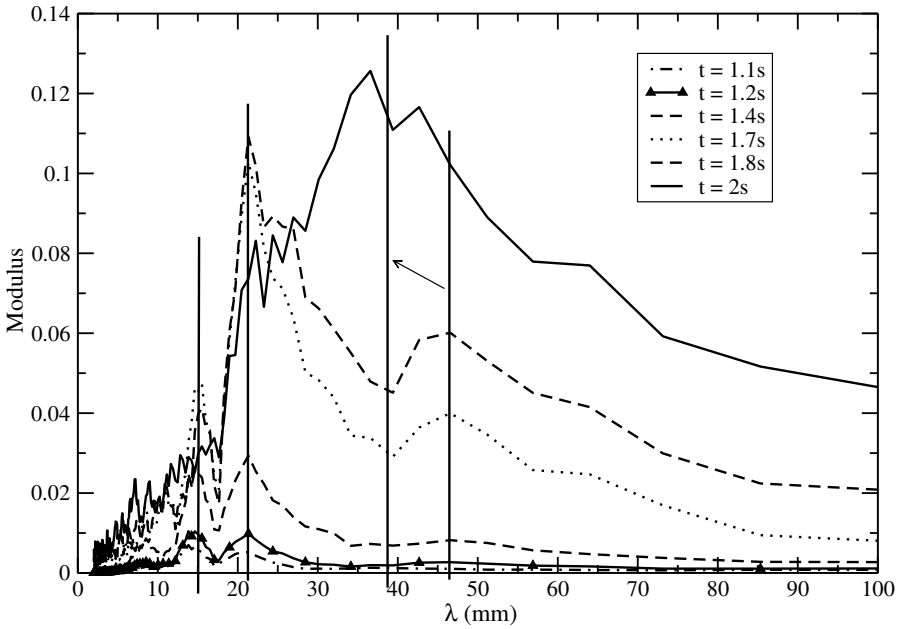

Fig. 10. FFT of the interface for $\sigma = 0$ N m^{-1}.

the spectral analysis of the interface for $\sigma = 0$ N m^{-1}. For this case, the results revealed a growing wavy flow earlier in the computation with a smaller wavelength than the previous case ($\sigma = 0.04$ N m^{-1}). In addition, there is not only one dominant wave-number along time, but several critical wave-numbers may be observed. Indeed, at early stages, the critical wavelength $\lambda_c \approx 15$ mm and $\lambda_c \approx 22$ mm can be observed. Afterward, the growing of the first one is stopped at $t \approx 1.7$ s, while the growing of $\lambda_c \approx 22$ mm slows down at $t \approx 1.7$ s and the wave disappears at $t \approx 1.8$ s (Fig. 10). From $t \approx 1.7$ s, when the growing of the dominant waves slows down, it gives rise to the growing of new waves with higher wavelength (Fig. 10). Fig. 10 also shows that this wave grows at $\lambda_c \approx 37$ mm, which is of the same order of magnitude as is the case with surface tension ($\lambda_c \approx 45$ mm). However, the amplitude of the most amplified wave-number is largely different from that obtained with surface tension (Fig. 8a), the ratio being larger than 2 (Figs. 8a and 10).

This mechanism of multiple wave-numbers may be attributed to an energy transfer between waves structures, which can pair each other or collapse to give rise to bigger structures with a larger wavelength. Therefore, even though the general trends given by the linear theory are assessed, the growing dynamics along the time may only be predicted by simulations.

Fig. 11 shows the fields of volume fraction for the two surface tensions and for different times. It is obvious that the growing dynamics starts earlier for $\sigma = 0$ N m^{-1}. Moreover, with no surface tension, wavy structures seem more likely to roll up and be brittle. This effect on the waves structure could not be predicted by the linear theory. The

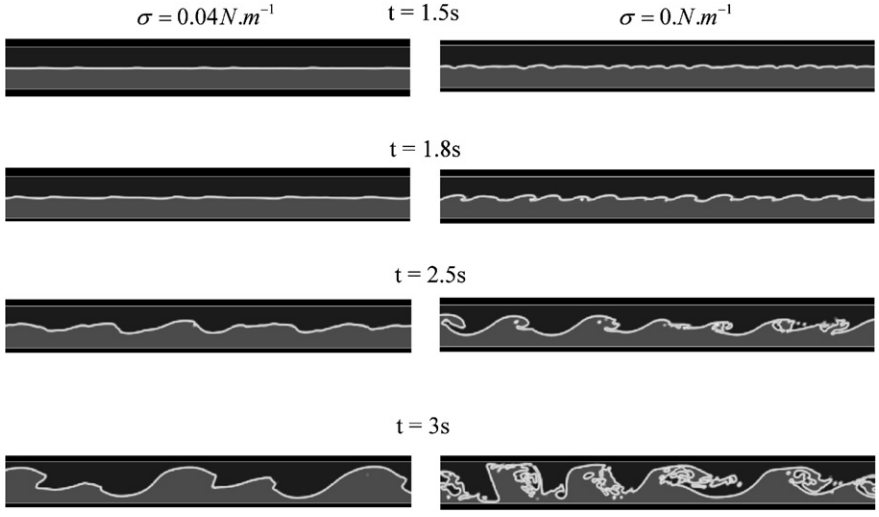

Fig. 11. Fields of volume fraction for $\sigma = 0$ N m^{-1} and $\sigma = 0.04$ N m^{-1}.

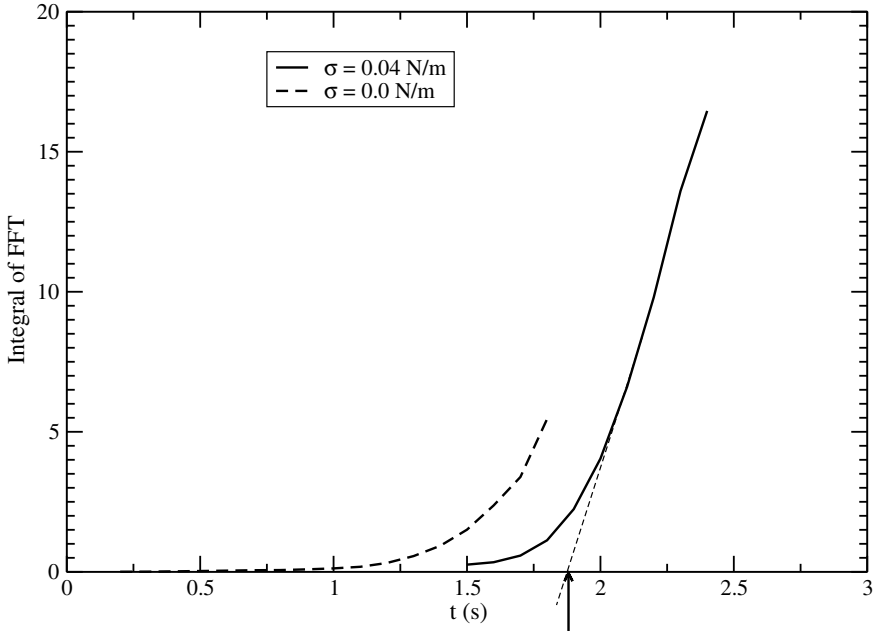

Fig. 12. Growing rate vs. time for different surface tensions.

offset in terms of times development of the structure can be more quantitatively evaluated with Fig. 12 that illustrates the integral of the previous FFT as a function of time. In the case with zero surface tension the time range of the plot is more limited due to the waves collapse, preventing a correct interface representation. The slope of the FFT integral can be understood as an image of the growing rate of the interface. From this figure, it is clear that the growing dynamics starts earlier as surface tension decreases, in accordance with the trend given by the linear theory. In addition, the different growing rates are roughly the same (same slope) (Fig. 12) as the surface tension is set to zero. The surface tension the does not have a significant effect on the growing rate, but rather on the time of onset of instability development and waves amplitude. These flow features cannot be easily deduced from the theory.

5.1.3. Effect of density ratio

In order to assess the influence of density ratio between the two fluids, two other cases have been simulated with FLUENT. In his paper, Thorpe (1969) noticed that the theory and its correction to take into account a smooth profile tends to underestimate t_0 and ΔU_c while the critical wave-number k_c still remains well predicted; he defined a parameter δ (Eq. (8)) to evaluate this effect. In our case, $\delta = 0.33$ and $\delta = 0.82$ have been tested for both $\sigma = 0.04$ N m^{-1} and $\sigma = 0$ N m^{-1}. Fig. 13 shows the fields of volume fraction for each density ratio and surface tension at $t = 1.5$ s. Increasing density ratio seems to have the same effect of decreasing the surface tension in terms of the time of onset of instabilities, but in this case structures do not have the same brittle feature. This means that by increasing the density ratio, smaller t_0 are obtained: it is clear from Fig. 13. In addition, by comparing the fields in Fig. 11 for both surface tensions, it is also clear that increasing density ratio provides a smaller wavelength or a larger wave-number. However, even though larger wave-numbers are predicted by the linear theory (Fig. 5a), the theory also predicts a larger t_0. In this case, numerical results and linear analysis are in contradiction. One possible explanation could be the that theory is valid for values δ small to negligible compared to the unity.

In addition, at average density ratio ($\delta = 0.33$) the surface tension effect is visible because the structure tends to easily roll up for $\sigma = 0$ N m^{-1}. In addition, at high-density ratio ($\delta = 0.82$), no significant differences can be observed according to the value of surface tension; at this ratio, the two fluids are almost separated. In this case, the

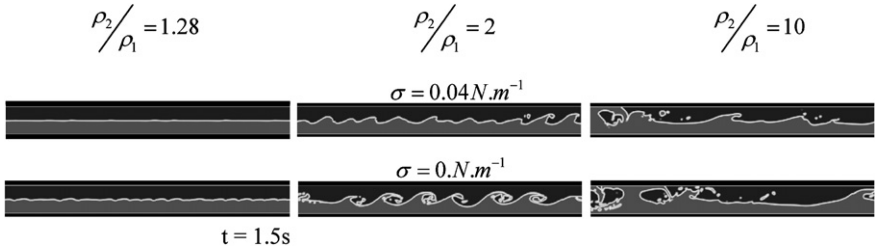

Fig. 13. Fields of volume fractions for different density ratio at $t = 1.5$ s.

dynamics is primarily dominated by density ratio. Further test should be performed to study the comparative effect of surface tension and density ratio to evaluate the different conditions where one or the other parameter dominates the dynamics and where both effects are in competition: this is out of the scope of the paper.

5.2. Comparison multi-field/VOF

5.2.1. A first study without surface tension

Since it is not in the spirit of a two-fluid model, the surface tension effects are not originally implemented in NEPTUNE_CFD. Consequently, FLUENT and NEPTUNE_CFD have to be firstly compared in a theoretical case without surface tension. Moreover, this study allows to evaluate NEPTUNE-CFD without any source term implemented which potentially could provide additional discrepancies compared to FLUENT according to the way the surface tension is included.

In this case, from the linear inviscid theory, the minimum of function F in Eq. (5) tends to infinity and becomes leveled, which means that a large range of critical smaller (than that for higher surface tensions) wavelengths are possible. In addition, with no surface tension the inviscid theory predicts a zero critical velocity and a time for onset of instabilities $t_0 = 0$ s. Fig. 14 illustrates the spectral analysis

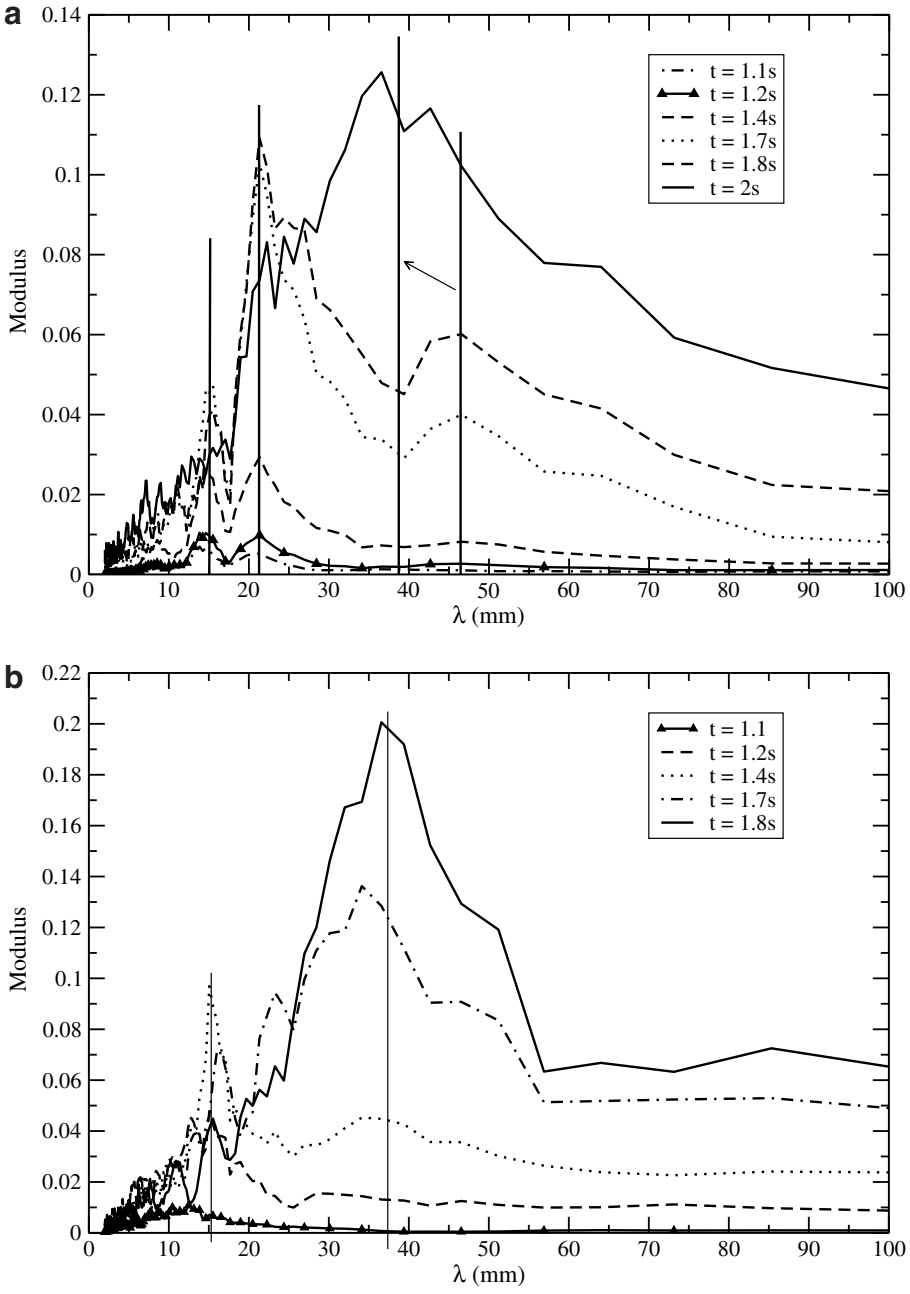

Fig. 14. FFT analysis: FLUENT (a) vs. NEPTUNE (b).

of the interface at several times between $t = 1.1$ s and $t = 1.8$ s. In the case of NEPTUNE_CFD, the location of the interface has been performed by interpolation during post-processing in order to determine the position of the $\alpha = 0.5$ isovalue. Compared to the results with $\sigma = 0.04\ \mathrm{N\ m^{-1}}$ (Fig. 8), Fig. 14a clearly indicates that the initial critical wavelength is much smaller for $\sigma = 0\ \mathrm{N\ m^{-1}}$. Furthermore, contrary to what is observed in Fig. 8, the most critical wavelength changes along the time: at initial stages, two modes seem to be excited $\lambda \approx 15$ mm and $\lambda \approx 22$ mm (Fig. 14a), while one critical wave-number is observed for all times for $\sigma = 0.04\ \mathrm{N\ m^{-1}}$ (Fig. 8). Also, Fig. 14a shows that the time for onset of the instability is smaller for $\sigma = 0\ \mathrm{N\ m^{-1}}$: for instance the FFT modulus, which is an image of waves amplitude, is clearly larger for $t = 1.1$ s and $\sigma = 0\ \mathrm{N\ m^{-1}}$ than for $t = 1.5$ s and $\sigma = 0.04\ \mathrm{N\ m^{-1}}$ (Fig. 8a). From these observations, VOF results seem to be in accordance with the conclusions of the linear theory. For this approach, as previously noted, two initial wave-numbers are excited from $t = 1.1$ s. The first one ($\lambda \approx 15$ mm) grows until $t = 1.7$ s (Fig. 14a) and decreases beyond this time. The second mode ($\lambda \approx 22$ mm) grows farther until $t = 1.8$ s even if this growing is slows down between $t = 1.7$ s and $t = 1.8$ s (Fig. 14a). At these times, another mode is grows and will become dominant ($\lambda \approx 37$ mm) at $t = 2$ s.

For NEPTUNE_CFD, the global dynamics is qualitatively the same but some differences can be observed (Fig. 14b). For the multi-field approach (Fig. 14b), there is only one dominant mode $\lambda \approx 15$ mm that grows until $t = 1.4$ s. Beyond this time, the modulus of this mode decreases and gives rise to the growing of a second critical wavelength $\lambda \approx 37$ mm, which still grows at $t = 1.8$ s (Fig. 14b). One may notice that the latter mode is also the dominant mode for FLUENT but from $t = 2$ s (Fig. 14a). In addition, the modulus of this mode is larger for NEPTUNE_CFD.

Fig. 15 represents the integral of previous FFT as a function of time for both FLUENT and NEPTUNE_CFD. The slope of this curve may then be interpreted as an image of the waves growing rate. Fig. 15 clearly demonstrates the different growing dynamics between both approaches. For the VOF results, the first growing stage is relatively slow until 1.5 s and increases later. For the two-fluid approach the first stage is stiffer until 1.6 s. With time, the difference in terms of growing rates (slope) tends to level out even though growing rates provided by NEPTUNE_CFD remain globally larger over the whole time range. The dynamics is then shifted to lower times for NEPTUNE_CFD and it is quicker.

Fig. 16 illustrates an example of the axial velocity profiles plotted along a radial line $x = 0$ for $t = 0.9$ s (a) and $t = 2.0$ s (b) obtained from FLUENT and NEPTUNE_CFD. For each time, the global shapes of the profiles are in good agreement. However, some discrepancies can be observed in high gradient regions (interface, walls), especially near the interface. This discrepancy comes from the difference in the waves amplitudes and wavelength calculation; and then in the different interface location given by both codes. In addition, at $t = 2.0$ s (Fig. 16b), a difference of about 7.5% is observed in the peak velocity because the waves have grown and have more influence on the core flow upside and downside of the interface; the influence was negligible for $t = 0.9$ s where waves amplitudes were small.

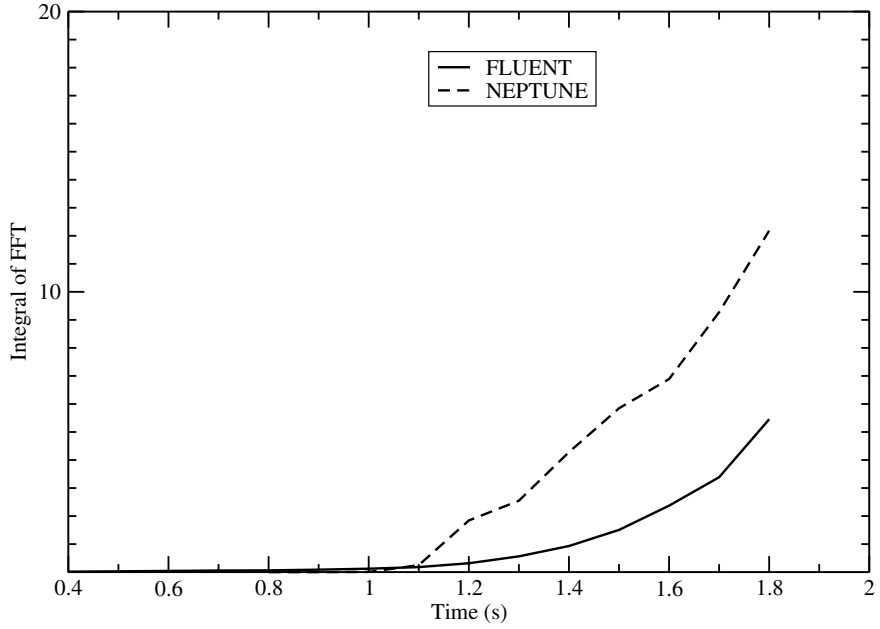

Fig. 15. Growing rates: FLUENT vs. NEPTUNE.

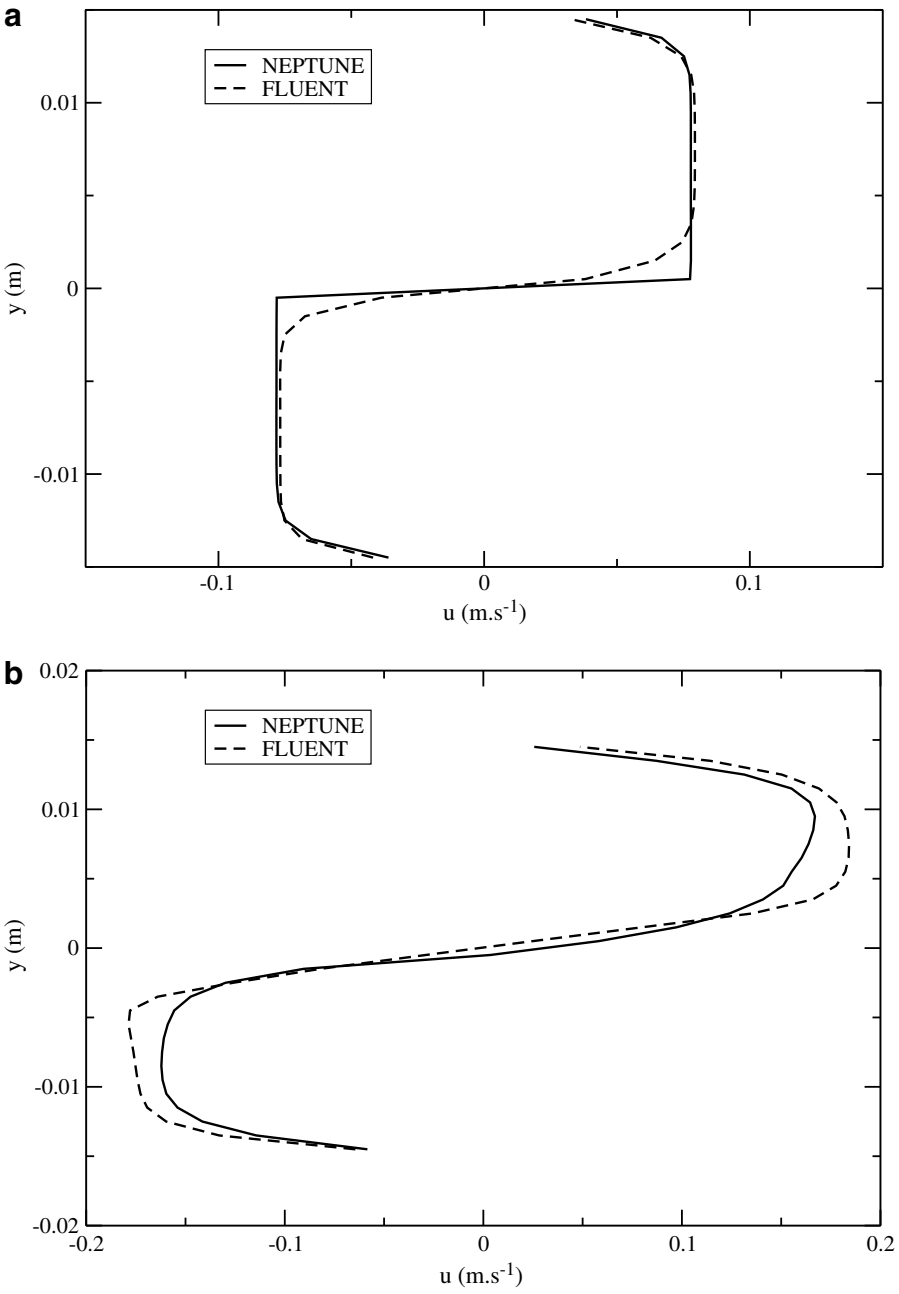

Fig. 16. Radial velocity profiles: FLUENT vs. NEPTUNE.

5.2.2. Implementation of surface tension in a multi-field model

In order to achieve a more relevant assessment of NEPTUNE_CFD to compute wavy stratified flows, the implementation of surface tension effects is required. In the most general view of a full-multi-field approach each phase may have its own properties, velocities, temperature and pressure fields. Velocity differences can be induced for instance by density differences. Temperature differences may be induced from a time lag of energy transfer between phases at the interface as thermal equilibrium is reached. Finally, pressure none-equilibrium may come from surface curvature between phases.

Source terms can then be added to model interactions between the fields. In a single-field approach under thermal equilibrium, velocities are assumed equal and friction terms (drag) are assumed equal and opposite in sign. Since a single pressure field is supposed, an extra source term is required to model surface tension at the interface. This method is used in the VOF technique. Surface tension which is actually a linear force or a surface energy is modeled as a source term F_{s_i} in the momentum equation (Eq. (11)). Therefore, the original formulation is cast in terms of a volume force acting in the cells containing the interface. The detailed derivation of this volumetric force can be found in Brackbill et al. (1992). In Eq. (11), this term is written for the direction *i*:

$$F_{s_i} = (\sigma\kappa \cdot \nabla\alpha_k)_i \tag{20}$$

where σ and κ represent the surface tension coefficient and the surface curvature. The curvature of the interface shape κ is defined in terms of the divergence of the unit normal vector:

$$\kappa = \nabla \cdot \hat{n} \quad \text{with } \hat{n} = \frac{n}{|n|} \tag{21}$$

$$n = \nabla\alpha_k \tag{22}$$

In NEPTUNE_CFD a multi-field but a single pressure assumption is used. In this framework, surface tension effects should be included as additional source terms. The continuum surface force (Brackbill et al., 1992) is used in the same spirit of the VOF approach. The curvature is calculated numerically by applying a smoothing method based on iterative geometric projections. The numerical parameters of the method have been adjusted from several basic test cases (sphere, ellipse and cylinder) to analytically validate the shape of the interface.

However, the volume force is split between the two phases occupying the cell:

$$F^k_{s_i} = (\beta_k \sigma\kappa \cdot \nabla\alpha_k)_i \tag{23}$$

where β_k is an averaged factor for the phase k that must satisfy the following necessary condition:

$$\sum_k \beta_k = 1 \tag{24}$$

This condition ensures consistency when kinetic equilibrium is assumed to derive the single mixture momentum equation since $\nabla\alpha_1 = -\nabla\alpha_2$. Two different models have been tested for the coefficient β_k. The first approach (mass formulation) is based on the fact that the surface tension source term for a cell is distributed between the two phases proportionally to the average mass in the cell:

$$\beta_k = \frac{\alpha_k \rho_k}{\sum \alpha_i \rho_i} \tag{25}$$

The second approach (volume formulation) is based on a volume averaging in the cell:

$$\beta_k = \alpha_k \tag{26}$$

The correctness of the implementation has been checked by calculating the pressure jump across a spherical bubble, which can be analytically calculated by $\Delta P = 2\sigma/R$. These two approaches have also been compared on the basis of the FFT analysis of the interface obtained during the time of the simulation of the Thorpe experiment (Fig. 17). As far as the wave dynamics is concerned, both formulations gave very similar results, so only results with the mass formulation have been compared to VOF. However, for very high-density ratios, both formulations should be carefully assessed.

Fig. 18a and b presents the results obtained with NEPTUNE_CFD with the implementation of surface tension mentioned above (mass formulation). The dash–dot lines represent running averages as illustrated in Fig. 8a and b. These results should be compared to those obtained by the VOF method (Fig. 8a and b) and also those obtained by NEPTUNE_CFD in the case without surface tension (Fig. 14b). From the time range 1.5–2 s, a dominant wave grows for $\lambda_c \approx 33$ mm. During this period, the same FFT given by FLUENT did not provide clear results (Fig. 8a), because the maximum was roughly located at $\lambda_c = 45$ mm, but the FFT peaks were wider in the range of $\lambda_c = 25$–55 mm. The Thorpe observations were in the range of $\lambda_c = 25$–45 mm. In addition, at $t = 1.5$ s, the amplitude of

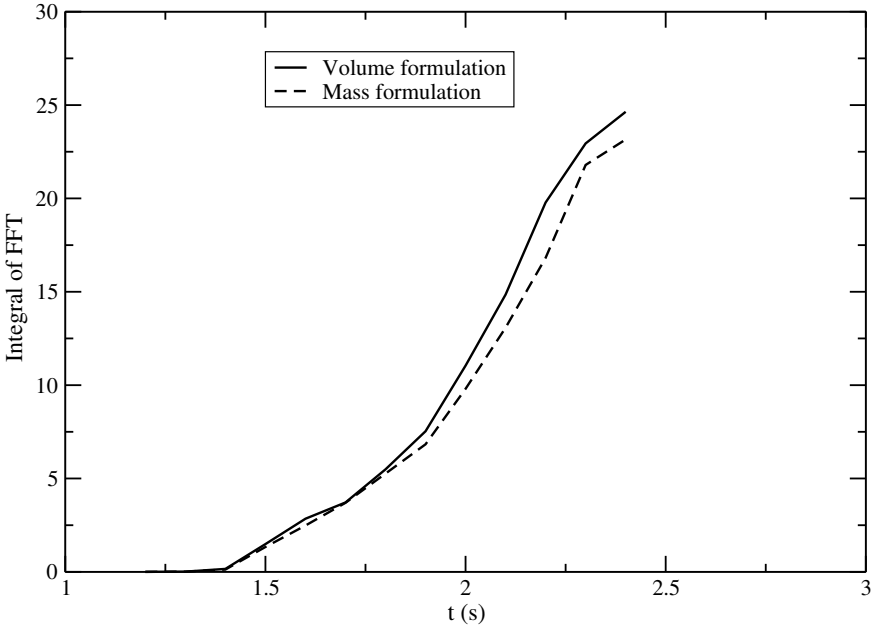

Fig. 17. Comparison of two surface tension formulations.

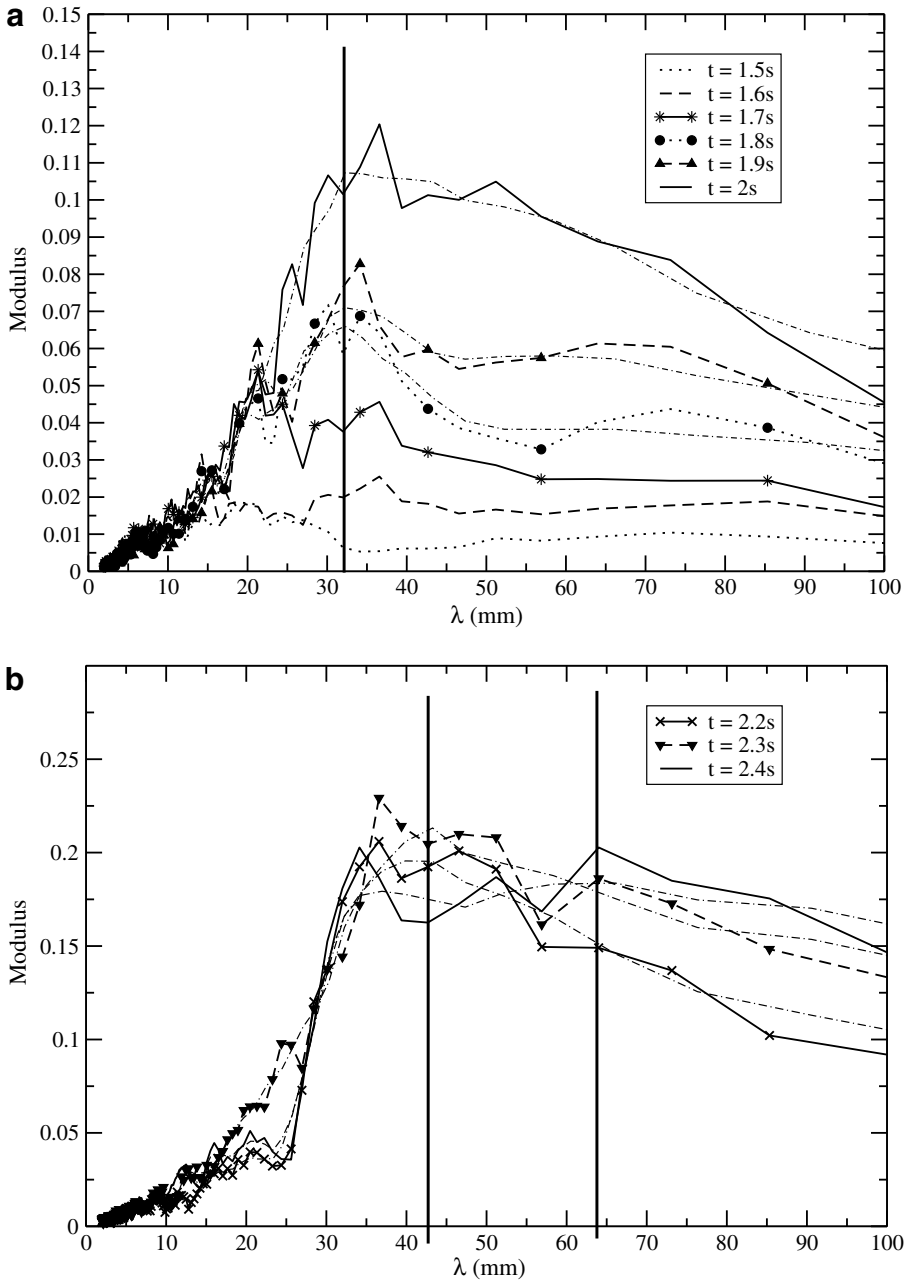

Fig. 18. Spectral analysis of the interface. The Thorpe experiment with surface tension implemented in NEPTUNE_CFD.

the critical wave-number given by NEPTUNE_CFD (Fig. 18a) is twice the value provided by FLUENT (Fig. 8a): the initial growing rates are then very different in both codes. At later times between 2 and 2.4 s, the critical wave-number provided by NEPTUNE_CFD is shifted at $\lambda_c \approx 43$ mm up to 2.3 s (Fig. 18b), which is roughly the value given by FLUENT over the total observed time range ($\lambda_c \approx 45$ mm). However, from $t = 2.3$ s, a mode at $\lambda_c \approx 65$ mm grows and tends to become dominant at $t = 2.4$ s and later. The growing of the mode $\lambda_c \approx 45$ mm then stops at this time, which is in agreement with Thorpe observations. This feature was not observed in FLUENT where the same critical wave-number $\lambda_c \approx 45$ mm still grows for this time range (Fig. 8b). Moreover, the amplitude of the most amplified wave-number at $\lambda_c \approx 45$ mm predicted by both codes (Figs. 8b and 18b) is almost the same contrary to the initial growing stage 1.5–2 s. This result was not observed in the case of zero surface tension. Results with surface tension appear to be in closer agreement between both methods than those obtained without surface tension. In the latter case, other terms that are not explicitly modeled in NEPTUNE_CFD such as interphase drag could play a more important role.

These observations may be understood by the comparison of the growing rates. Fig. 19 illustrates the different growing rates obtained with and without surface tension

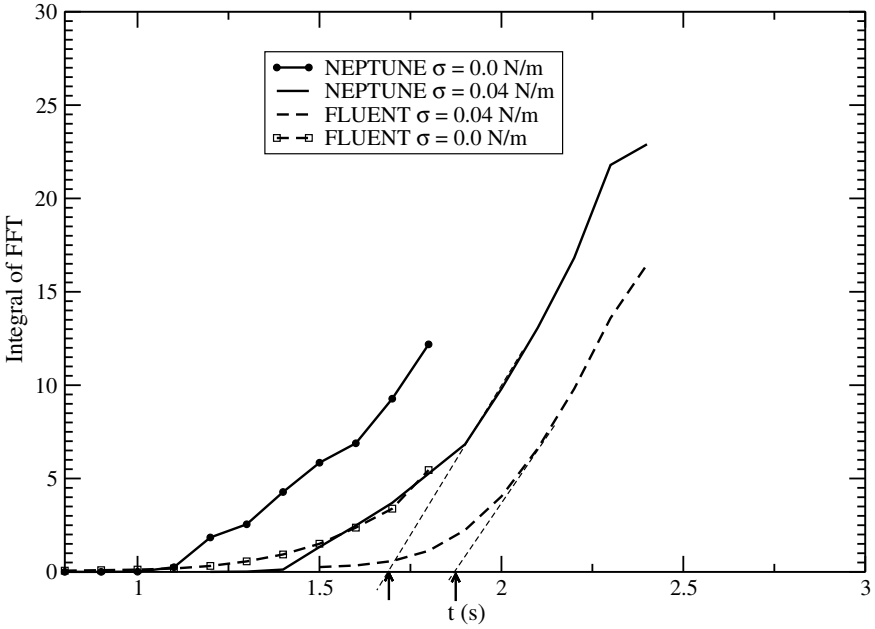

Fig. 19. Comparison of the growing rates obtained with the VOF and the two-fluid approaches.

by both approaches. As previously noted, this figure shows that surface tension do not have a significant effect (for a given approach) on the different growing rates (slopes) but rather on the time shifting of the dynamics. Also, it is clearly shown that the dynamics starts earlier with no surface tension in both cases. However, for the case with surface tension, both growing rates are similar beyond the initial growing stage and up to $t = 2.3$ s: the curves are mainly time shifted contrary to the case without surface tension where the growing rates were even different along the whole time range.

From this time ($t = 2.3$ s), the growing rate predicted by NEPTUNE_CFD significantly decreases compared to that provided by FLUENT: this is observed in Fig. 18b where the amplitude of the most amplified wave at $\lambda_c \approx 45$ mm is shown decreasing. This explains why the waves amplitude obtained by the VOF method could take back its delay and reach roughly the same value beyond $t = 2.3$ s.

The time of onset of the significant growing is estimated to be $t_0 = 1.67$ s for NEPTUNE_CFD compared to $t_0 = 1.86$ s for FLUENT which is in rather good agreement with Thorpe's observations and linear analysis (Table 1). This time shifting could also explain why a new critical wave-number rises at $t = 2.4$ s for NEPTUNE_CFD (Fig. 18b), the dynamics predicted by FLUENT being late (Fig. 8b). However, this point should be addressed and other possible causes such as the implementation of different drag terms between phases should be tried out.

Finally, if these results are compared to those obtained by the same multi-field approach without surface tension (Fig. 14b), the same conclusion as the VOF case can be drawn: the surface tension does not have a significant effect on the most amplified wave-number ($\lambda_c \approx 33$–37 mm for $t = 1.8$ s, Figs. 14b–18a), but rather on its amplitude. As previously noted for the VOF case, the amplitude of this most amplified wave-number is more than two times larger for the case without surface tension (at $t = 1.8$ s $\|\lambda_c\| \approx 0.2$ in Fig. 14b, while $\|\lambda_c\| \approx 0.07$ at $t = 1.8$ s in Fig. 18a).

6. Concluding remarks

In this paper, we present first results concerning the assessment of NEPTUNE_CFD, a new European research code for modeling two-phase flows relevant to nuclear safety. The proposed benchmark, relevant to a pressure thermal shocks (PTS) scenario, relies on the Thorpe experiment to characterize the wavy dynamics of two immiscible fluids. This is a rather good challenge for NEPTUNE_CFD, because the two-fluid approach is not the most suitable one for the modeling of free surface flows compared to VOF. Nevertheless, this approach has to be used in a PTS scenario because of the wide variety of flows encountered (impinging jets, bubbly flows, wavy, etc.).

The first results showed that FLUENT is able to provide rather good results compared to experimental data of Thorpe. Moreover, these tests allowed to highlight the role of the surface tension and density ratio on the wave structure and development. Those results were in accordance with the trends given by the linear analysis, but were able to provide more details on the growing dynamics. For instance it was observed that the surface tension has no significant effect on the most amplified wave-number but rather on its amplitude and the global dynamics. However, some results concerning the effect of the density ratio were in contradiction with the theory that becomes limited according to the value of δ.

Afterward, both the VOF and the two-fluid approach have been compared in a case without surface tension. This

test case was useful because it can provide general trends and differences without any source terms added in both codes. These preliminary results highlighted a time shifting in the dynamics, different growing rates and dynamics, but the most amplified mode was roughly for the same wave-number.

In addition, in order to be able to compute stratified flows, surface tension effects had to be implemented in NEPTUNE_CFD since the approach relies on a two-field single pressure approach. A mass and a volume formulation in respect of the force splitting within a control volume have been proposed. Those two formulations did not present significant differences for the Thorpe case. This implementation allowed the comparison with the results obtained with the VOF approach. In those conditions, the same time shifting phenomenon was still observed, but the growing rates values were in better agreement beyond the initial growing stage. In spite of this time shifting, the time of onset of the dynamics still remained in good agreement compared to the theory and Thorpe observations. In addition, the most amplified wave-number was also well predicted by the multi-field method and its amplitude was in rather good agreement between both approaches. Concerning the time from which Thorpe observed the stoppage of this wave growing, NEPTUNE_CFD even provided better results.

Future work will deal with the assessment of different drag terms suited for separated flows in order to resolve this time shifting, and also possibly to explain the more important differences noted during zero surface tension tests. However, the results showed it should the be possible to get an acceptable description of complex stratified flows involving surface tension effects with a general multi-field code which is originally more suitable for dispersed flows. Furthermore, the gain in terms of CPU time with NEPTUNE_CFD is very significant, probably because of the time consuming geometric reconstruction algorithm used for the VOF method.

Acknowledgements

The NURESIM project is partly funded by the European Commission in the framework of the Sixth Euratom Framework Program (2002–2006). Authors also wish to acknowledge François Vercheval from the TERM division for the different drawings of this paper.

References

Ansari, M.R., 1998. Numerical analysis for slugging of steam-water stratified two-phase flow in horizontal duct. Fluid Dyn. Res. 22, 329–344.

Bartosiewicz, Y., Seynhaeve, J.-M., 2006. Numerical investigation on the Kelvin–Helmholtz instability in the case of immiscible fluids. In: 13th International Conference on Fluid Flow Technologies. Budapest, Hungary.

Biberg, D., Halvorsen, G., 2000. Wall and interfacial shear stress in pressure driven two-phase laminar stratified pipe flow. Int. J. Multiphase Flow 26, 1645–1673.

Brackbill, J.U., Kothe, D.B., Zemach, C., 1992. A continuum method for modelling surface tension. J. Comp. Phys. 100, 335–354.

Chandrasekhar, S., 1961. Hydrodynamics and Hydromagnetic Stability. Oxford University Press, Oxford.

Drazin, P.G., Reid, W.H., 1982. Hydrodynamics Stability. Cambridge University Press, Cambridge, MA.

Funada, T., Joseph, D.D., 2001. Viscous potential flow analysis of Kelvin–Helmholtz instability in a channel. J. Fluid Mech. 445, 263–283.

Hou, T.Y., Lowengrub, J.S., Shelley, M.J., 2001. Boundary integral methods for multicomponent fluids and multiphase materials. J. Comp. Phys. 169, 302–362.

Issa, R.I., 1986. Solution of implicitly discretized fluid flow equations by operator splitting. J. Comp. Phys. 62, 40–65.

Kim, H.J., Lee, S.C., Bankoff, S.G., 1985. Heat transfer and interfacial drag in countercurrent steam-water stratified flow. Int. J. Multiphase Flow 11, 593–606.

Lioumbas, J.S., Paras, S.V., Karabelas, A.J., 2005. Co-current stratified gas–liquid flow field on interfacial structure. Int. J. Multiphase Flow 31, 869–896.

Meignin, L., Gondret, P., Ruyer-Quil, C., Rabaud, M., 2003. Subcritical Kelvin–Helmholtz instability in a Hele–Shaw cell. Phys. Rev. Lett. 90 (23), 234502-1–234502-4.

Staquet, C., 1995. Two-dimensional secondary instabilities in a strongly stratified shear layer. J. Fluid Mech. 296, 73–126.

Staquet, C., 2000. Mixing in a stably stratified shear layer: two- and three-dimensional numerical experiments. Fluid Dyn. Res. 27, 367–404.

Tailtel, Y., Ducker, A.E., 1976. Model for predicting flow regime transitions in horizontal and near horizontal gas liquid flow. AICHE J. 22, 47–55.

Thorpe, S.A., 1969. Experiments on the instability of stratified shear flows: immiscible fluids. J. Fluid Mech. 39, 25–48.

Tiselj, I., Strubelj, L., Bajsic, I., 2004. Test-case No 36: Kelvin–Helmholtz instability. Multiphase Sci. Technol. 16 (1–3), 273–280.

Wallis, G.B., Dobson, J.E., 1973. The onset of slugging in horizontal stratified air water flow. Int. J. Multiphase Flow 1, 173–193.